ingegneria sismica
International Journal of Earthquake Engineering
Anno XLIII - Num. 1 - 2026

Hydrodynamic modeling study of filling flow behavior in magnesium alloy die-casting forming process

Li Ma[1,*] *and Yu Wang*[2]

[1] School of Aeronautical Materials Engineering, Xi'an Aeronautical Polytechnic Institute, Xi'an, Shaanxi, 710089, China
[2] School of Mechanical and Material Engineering, Xi'an University, Xi'an, Shaanxi, 710089, China

SUMMARY: *The study established the SPH method calculation model of smooth particle hydrodynamics for magnesium alloy die-casting filling process based on pure Lagrangian description, introduced the Monaghan boundary model to establish the boundary conditions of the cavity wall, and satisfied the boundary conditions of inflow by dividing the inflow area particles and fluid particles. On this basis, the establishment of surface tension model program, through the square droplet rounding calculations, bubble uplift case and underwater side injection square cavity simulation calculations, to verify the SPH method calculation of magnesium alloy die casting filling gas-biphasic flow simulation correctness. Findings derived from the computed data indicate that when the calculation time is at 0.37s, 0.58s and 1.65s, the outcomes show strong agreement with the experimental measurements, and the computed results align closely with the experimental data, thereby confirming the validity of the gas-liquid dual-phase flow framework of the SPH filling model. Comparing the injection outcomes against the simulation results, it is found that the pressure injection velocity exerts a notable influence on the mold-filling duration as well as cavity filling degree, and the faster the pressure injection speed is, the shorter the filling time is. The study provides theoretical basis and technical support for the deep understanding of magnesium alloy die casting filling flow mechanism and refinement of the die-casting process parameters to enhance the quality of magnesium alloy die casting products.*

KEYWORDS: *smooth particle hydrodynamics; pressure casting; numerical simulation; gas-liquid two-phase flow*

1 Introduction

In recent years, in response to the call for green development and energy saving and emission reduction, magnesium alloy, as a kind of green engineering structural material, has the advantages of light weight, good casting performance and dimensional stability, good tensile strength and flexural rigidity, good vibration damping, good electromagnetic interference suppression capability, etc., which is extensively employed across the sectors of automotive manufacturing, aerospace and aviation, electronic products, military weaponry, biomedicine and other fields to promote the sustainable development of various industries [1-5]. With the steady development of industry and the research on higher quality performance magnesium alloy and related production technology, magnesium alloy materials will have a broader

*mary830805@163.com
https://doi.org/10.65102/is2026352
Published: 30 April, 2026

development prospects.

Magnesium alloy die casting forming process of less chip-free process and can be recycled high utilization rate, very responsive to the current clean industry and energy saving and emission reduction call [6]. Among them, pressure casting techniques employ high pressure alongside elevated velocity to drive molten or semi-solid liquid metal into the mold cavity within an extremely brief timeframe, completing the entire cavity-filling sequence [7]. Because of the die casting filling speed can be controlled, filling smooth, and can be under pressure to make up the contraction, solidification, so you can get high dimensional accuracy of the castings, and has the casting quality is good, high productivity, suitable for magnesium, aluminum and other alloys castings of mass production [8-11]. Die casting production is generally used in horizontal cold-chamber casting equipment, and its ejection procedure control of its ejection can usually be divided into slow ejection process and fast ejection process. Slow injection process is mainly through the control of punch movement to regulate the liquid metal liquid in the pressure chamber movement state, in order to ensure that the liquid metal flow is smooth and in the punch movement process to minimize the gas involved and with the liquid metal together with the cavity filled [12-15].

In the actual die casting production process, filling flow behavior as a key production link, the behavior of molten material within the compression chamber throughout the movement process will directly affect the solidification of the die casting organization and mechanical properties, and ultimately affect the casting quality [16-18]. When the movement speed of the filling process is not reasonable, the air will be involved in the liquid metal, and finally enter the mold cavity, thereby compromising the integrity of the cast component, which constitutes one of the main reasons for the generation of porosity in die casting [19, 20]. And when the movement speed of the filling process is too slow, the metal liquid will solidify prematurely inside the die chamber, resulting in cold segregation defects [21, 22]. Based on this, examining the mold-filling flow pattern carries considerable research significance for pressure-casting forming procedures of magnesium alloys to improve the overall casting excellence castings.

Fluid mechanics, as an important branch in dynamics, mainly studies the state of motion of fluids in various occasions and the mechanical properties related to fluids [23]. In doing research on fluid mechanics, the fluid motion behavior is simulated by building mathematical models so as to predict the fluid state, analyze the temperature distribution and fluid defects, and thus reduce the industrial production cycle and optimize the cost [24-26]. Therefore, hydrodynamic modeling is an important tool to study the filling flow behavior within magnesium alloy components during pressure casting and forming.

With respect to the simulation involving magnesium alloy casting process, literature [27] revealed the thermal transfer, phase transformation, and compositional redistribution behaviors of magnesium alloy electromagnetic direct current casting process with an axially symmetric two-dimensional computational framework, and under the influence of the applied magnetic field, the thermal condition of casting process is uniformly distributed, the solidification rate is accelerated, and segregation is reduced in the casting billet cross-section. Literature [28] used NovaFlow&Solid software package for numerical casting simulation of vacuum core casting process to manufacture magnesium alloys, pointing out that the pressure-assisted forming procedure with a rise in vacuum pressure, can obtain better filling effect and high quality product quality. Fewer studies for magnesium alloy die casting process for hydrodynamic modeling, so as to study the die casting in the mold filling flow behavior.

However, the computational modeling of cavity-filling flow in pressure casting is more widely studied. Literature [29] combined the water model experiment and numerical simulation to analyze the interfacial flow characteristics of the fill pattern within the reduced-pressure forming sequence of magnesium alloys, and clarified the influence of different gate shapes on

the free surface flow pattern of the mold-filling progression. Literature [30] numerically simulated the liquid metal injection and filling phases of high-pressure die casting by adopting the volume fluid method, and introduced the Euler-Lagrange framework and water modeling experiments to track and simulate the changes in flow patterns and droplet formation. Literature [31] simulated the entire high-pressure casting procedure of the material with the assistance of digital simulation techniques for the forming sequence, drawing upon computer-aided engineering and adjusted the operational variables of the casting workflow on the foundation of thermocouple data acquisition and thermal imaging of the heat distribution across the surface of the casting. Literature [32] applied generalized finite difference method and a semi-implicit Chorin-Uzawa pressure-velocity decoupling algorithm for numerical prediction of complex three-dimensional open-boundary flow in metal casting process during mold filling, which is a network-free form of the method. Literature [33] simulated the cavity-filling flow pattern of alloy rheological pressure casting process for different range of plunger speeds by Flow-3D CastTM software, high speed plunger leads to bubble formation while slow filling reduces the air retention in the overflow zone and reduces the bubble formation.

Literature [34] proposed a numerical simulation method for casting filling process based on smooth particle fluid dynamics and finite element, which realized fully coupled flow-heat-stress simulation, and the computational efficiency and accuracy are suitable for casting engineering environment. Literature [35] used a flow field visualization experiment oriented to computational fluid dynamics to simulate and validate the filling behavior in pressure-assisted die casting, visually observing the mold-filling trajectory and predicting the porosity at different locations under different pouring speeds. Literature [36] innovated a filling visualization dynamic characterization experiment for alloy die casting process, which is based on computational fluid dynamics and reveals the effect of different liquid metal injection rates on gas-induced voiding defects. Literature [37] simulates the transport behavior of molten material and gas throughout the injection stage in the foundry industry by means of a lattice Boltzmann model, which correctly describes the effects such as bubble formation and air backpressure, and has lower arithmetic memory requirements than the dual-phase flow finite volume framework. The lattice Boltzmann approach, on the other hand, is a computational fluid dynamics approach based on mesoscopic simulation scales. Literature [38] analyzed the flow behavior of metallic liquid and oxide film distribution defects under different filling speeds by numerical fluid dynamics modeling and experimental validation in the alloy reduced-pressure casting charging procedure, so as to determine the microstructure and mechanical properties of the alloy.

This experimental validation technique for the charging flow behavior. Literature [39] through a casting process simulation software - Click2cast casting filling and solidification process analysis and experimental validation, to assist in reducing the production process of casting defects and test costs, and thus reduce the casting failure rate. Literature [40] with the help of pressure chamber monitoring networks, injection punch velocity and positional transducers to collect die casting machine equipment data, the use of visual inspection, X-ray inspection and microscopic analysis of three methods to evaluate the casting quality of die casting process. Literature [41] using two-phase flow model and X-ray radiography observation technology two methods, low pressure casting alloy process under different die casting speed of filling alongside the evolution of material performance indicators throughout the computational modeling, examining how the gate velocity progression shows a sharp increase - smooth - slowly increasing trend. Literature [42] used micro X-ray computed tomography and semiconductor sensors for real-time detection of casting defects (e.g., air holes and inflated voids) inside the die-cast samples of relative metal alloys. Literature [43] integrated water simulation experiments, MAGMASOFT flow simulation, and X-ray computed tomography to

quantify the nucleation and growth of gaseous inclusions under elevated-pressure vacuum-assisted casting conditions across different alloys as a way to reduce the number of air voids in production.

First of all, through the basic theory of smooth particle hydrodynamics method, this paper establishes the computational model of SPH method for die-casting process. And for the boundary problem in the three-dimensional space of SPH, the Monaghan boundary model is introduced to establish the boundary conditions of the cavity wall, and the incoming boundary conditions are satisfied by dividing the incoming area particles and fluid particles. Then the vapor-melt dual-phase transport calculation program dedicated to SPH charging was established by introducing the surface tension model and discretizing the gas-liquid two-phase governing equation of the charging process. Finally, the charging process was simulated with the same process parameters, with the injection outcomes subsequently benchmarked against the computed findings so as to verify the three-dimensional mathematical model.

2 SPH-based hydrodynamic modeling of magnesium alloy die casting filling pattern

2.1 SPH Fundamentals

SPH method, the full name of smooth particle hydrodynamics, is a Lagrangian-based meshless numerical simulation computation method, which has a great deal of flexibility and space for use in the engineering field.The SPH method, in principle, is to discretize the continuum in the form of a mesh, and then focus the physical quantities of the mesh to the center of the mesh on the bulkless mass, that is, the way to replace the problem domain with more than one particle. There is no line or grid connection between all the particles, and the iterative operation takes one particle as the reference and searches for other particles in the domain of influence, which become paired particles. The transfer of physical quantities between paired particles is mainly determined by the establishment of the SPH particle approximation and the choice of the kernel function. The choice of the kernel function determines the degree of influence of a particle on the benchmark particle, and the correct construction of the kernel function directly affects the accuracy of the calculation by influencing the support domain in the calculation process.

2.2 SPH approximation and kernel function

2.2.1 Integral approximation

First, the function $f(x)$ is written out in the SPH method in terms of the definition of the integral representation as follows:

$$f(x)=\int_{\Omega} f(x')\delta(x-x')dx' \tag{1}$$

In the above equation, f is a function with three-dimensional coordinates $\mathbf{x}$ as the independent variable, where the Dirac function $\delta(x-x')$ has a mathematical nature in a particular case:

$$\delta(x-x')=\begin{cases}1, & x=x'\\ 0, & x\neq x'\end{cases} \tag{2}$$

In Eq. Ω is the integral domain covering $\mathbf{x}$. The above formula, with the Dirac function applied, must be a strictly continuous function for the integral representation as long as the function $f(x)$ is a continuous function. We use the smooth function (also known as the kernel function) $W(x-x',h)$ to make an alternative to the Dirac function $\delta(x-x')$ in the above equation, and the integral expression for $f(x)$ can be rewritten as:

$$f(x) \approx \int_{\Omega} f(x') W(x-x',h)\, dx' \tag{3}$$

where h is the smooth length, and his main role is that he can change the domain of influence of the smooth kernel function. In the SPH formulation, we often use angular brackets to represent the kernel approximation operator, so the above equation is rewritten as:

$$\langle f(x) \rangle = \int_{\Omega} f(x') W(x-x',h)\, dx' \tag{4}$$

The SPH smooth kernel function must firstly be an even function associated with $\mathbf{x}$, and secondly, it needs to satisfy three important conditions: the regularization condition and the integral value of the integral function is 1; the smooth length tends to 0 with Dirac function property; and the tightness condition and the value of the smooth function outside the support domain is 0.

The scattering law is shown in Eq. First, the $f(x)$ in the above equation is replaced by the gradient operator $\nabla \cdot f(x)$, and then the scattering law is transformed on the column coordinate system:

$$\iiint_{V} \nabla \cdot F dV = \iint_{S} F dS \tag{5}$$

$$\langle \nabla \cdot f(x) \rangle = \int_{\Omega} \left[\nabla \cdot f(x') \right] W(x-x',h)\, dx' \tag{6}$$

$$\begin{aligned} \langle \nabla \cdot f(x) \rangle = & \int_{S} f(x') W(x-x',h) \cdot \vec{n} dS \\ & - \int_{S} f(x') \cdot \nabla W(x-x',h) \cdot \vec{n} dx' \end{aligned} \tag{7}$$

where $\vec{n}$ is the unit normal vector over the S-plane solution domain.

2.2.2 Particle approximation method

Immediately following the SPH integral approximation is the discrete particle estimation approach, the abstract expression employed to transform the SPH integral representation into the form of all particles in the domain of support of the nuclear function of the approximation of the superposition of the form of one by one, can also be more directly described as the support of every particle contained within the computational region in terms of the nuclear weighting formulation.

Using the volume ΔV_j of the particle to integrate the infinitesimal microelement dx' at the approximating particle j, then the particle's mass m_j is expressed as:

$$m_j = \rho_j \Delta V_j \tag{8}$$

So the integral expression of $f(x)$ written discretized particle approximation is:

$$\begin{aligned} f\left(x\right) &= \int_{\Omega} f\left(x'\right) W\left(x - x', h\right) dx' \approx \sum_{j=1}^{N} f\left(x_j\right) W\left(x - x', h\right) \Delta V_j \\ &= \sum_{j=1}^{N} f\left(x_j\right) W\left(x - x', h\right) \frac{1}{\rho_j} \left(m_j\right) \end{aligned} \tag{9}$$

The approximation of the particle i-function is finally obtained:

$$\langle f(x_i) \rangle = \sum_{j=1}^{N} \frac{m_j}{\rho_j} f(x_j) W_{ij} \tag{10}$$

Similarly, the above particle approximation of the spatial derivative of the solution function using the SPH method yields the expression:

$$\langle \nabla \cdot f(x_i) \rangle = -\sum_{j=1}^{N} \frac{m_j}{\rho_j} f(x_j) \cdot \nabla_i W_{ij} \tag{11}$$

This one:

$$\nabla_i W_{ij} = \frac{x_i - x_j}{r_{ij}} \frac{\partial W_{ij}}{\partial r_{ij}} = \frac{x_{ij}}{r_{ij}} \frac{\partial W_{ij}}{\partial r_{ij}} \tag{12}$$

In the above equation r_{ij} is the paired-particle spacing, and since here $\nabla_i W_{ij}$ is associated with particle i, it is important to remove the negative sign from Eq:

$$\langle \nabla \cdot f(x_i) \rangle = \sum_{j=1}^{N} \frac{m_j}{\rho_j} f(x_j) \cdot \nabla_i W_{ij} \tag{13}$$

2.2.3 Kernel function

A kernel function is defined as a functional formula which is expressed in an integral form on top of the theoretical basis of using Taylor series expansions. This function not only confirms the size of the domain of support for each search and governs the mathematical profile of the interpolation scheme, while simultaneously serving as the most important parameter for determining the accuracy of the solution of the SPH program. There are many kinds of kernel functions, such as bell function, Gaussian function, cubic spline function, quadratic spline function and quintuple spline function, etc. Within the scope of this study, the cubic spline basis function has been selected to fulfill the role of the kernel function, and accordingly we take the cubic spline function as the kernel function.

Cubic spline function:

$$W\left(R,h\right)=\alpha_d\begin{cases}\dfrac{2}{3}-R^2+\dfrac{1}{2}R^3, & 0\le R\le 1\\ \dfrac{1}{6}\left(2-R\right)^3, & 1<R<2\\ 0, & R\ge 2\end{cases} \tag{14}$$

Specific forms of first order derivatives:

$$W'\left(R,h\right)=\alpha_d\begin{cases}-2R+\dfrac{3}{2}R^2, & 0\le R\le 1\\ -\dfrac{1}{2}(2-R)^2, & 1<R<2\\ 0, & R\ge 2\end{cases} \tag{15}$$

2.3 Modeling of die casting mold filling process by SPH method

2.3.1 SPH method for discretization of control equations

Particle summation form:

$$\langle f(x_i)\rangle=\sum_{j=1}^{N}\frac{m_j}{\rho_j}f(x_j)W\left(x_i-x_j,h\right) \tag{16}$$

Similarly, for the gradient function, the gradient of the kernel function can be used to construct a summation representation:

$$\langle\nabla f(x_i)\rangle=\sum_{j=1}^{N}\frac{m_j}{\rho_j}f(x_j)\nabla W\left(x_i-x_j,h\right) \tag{17}$$

where: N is the total number of particles in the support domain of particle i (excluding particle i). Equations (16) and (17) enable the scalar quantity and its spatial derivative at any given location in the space to be expressed as an influence-weighted aggregation of the corresponding scalar quantities belonging to the neighboring particles residing within the support domain.

Using Eqs. (16) and (17) to discretize and organize the control equations under the Lagrangian description, the SPH representations of the mass conservation equation, the equation governing momentum transfer, and the thermal energy balance equation can be obtained:

$$\frac{d\rho_i}{dt}=\sum_{j=1}^{N}m_j v_{ij}^{\beta}\frac{\partial W_{ij}}{\partial x_i^{\beta}} \tag{18}$$

$$\frac{dv_i^{\alpha}}{dt}=-\sum_{j=1}^{N}m_j\left(\frac{p_i}{\rho_i^2}+\frac{p_j}{\rho_j^2}\right)\frac{\partial W_{ij}}{\partial x_i^{\alpha}}+\sum_{j=1}^{N}m_j\left(\frac{\mu_i\varepsilon_i^{\alpha\beta}}{\rho_i^2}+\frac{\mu_j\varepsilon_j^{\alpha\beta}}{\rho_j^2}\right)\frac{\partial W_{ij}}{\partial x_i^{\beta}} \tag{19}$$

$$\frac{dU_i}{dt}=\frac{1}{2}\sum_{j=1}^{N}m_j\left(\frac{p_i}{\rho_i^2}+\frac{p_j}{\rho_j^2}\right)v_{ij}^{\beta}\frac{\partial W_{ij}}{\partial x_i^{\beta}}+\frac{\mu_i}{2\rho_i}\varepsilon_i^{\alpha\beta}\varepsilon_j^{\alpha\beta} \tag{20}$$

where: m, ρ, v, p, U represent the mass, density, velocity, pressure and internal energy of the particle, respectively; the subscripts i and j represent the number of the interacting pair of particles, and the subscript i for each variable means that it belongs to the particle i, while the subscript j means that it belongs to the particle j; v_{ij}^{β} is the relative velocity of particle i and particle j; $\varepsilon^{\alpha\beta}$ is the strain rate tensor function; the superscripts α and β denote the direction of the coordinates; μ is the coefficient of dynamical viscosity; t is the time variable.

2.3.2 Wall boundary conditions

In the SPH analysis of pressure-casting mold-filling procedures, the particleization of the mold cavity wall surface is required, so as to provide wall boundary conditions for the molten metal injection. Owing to the complexity of the mold cavity, the establishment of wall boundary conditions needs to have a certain degree of flexibility to ensure the fitting of complex cavity walls. One method is to establish phantom particles symmetrical to the boundary through the particles near the boundary, assign all the virtual particles with all the variable values equal to the value at the boundary, and integrate along the special boundary formed by the virtual particles to calculate the value at the internal particles. Since the virtual particles used in this method need to be obtained by mirroring the particles close to the wall through the wall, it can be conveniently implemented in some simple geometric models, but the geometry of the mold cavity wall is often very complex, and the creation of virtual particles is very difficult.

Using the boundary repulsive force model, a layer of wall particles is arranged on the fixed wall surface for applying strong repulsive force to the neighboring boundary particles, thus preventing the adjacent boundary particles from penetrating the boundary. This method only requires a certain density of particles on the surface of the mold cavity, which is flexible and easy to implement. The mathematical model of the repulsive force F_{ij} is:

$$F_{ij}=\begin{cases}D\left[\left(\dfrac{r_0}{r_{ij}}\right)^a-\left(\dfrac{r_0}{r_{ij}}\right)^b\right]\dfrac{x_{ij}}{r_{ij}^2}, & \dfrac{r_0}{r_{ij}}\le 1\\ 0, & \dfrac{r_0}{r_{ij}}>1\end{cases} \tag{21}$$

where: the parameters a and b are generally taken to be 12 and 4, respectively; D is taken to be of an order of magnitude equal to the square of the maximum value of the velocity; and r_0 is the cutoff radius, which is generally taken to be a value similar to the initial particle spacing.

2.3.3 Inflow boundary conditions

With the aim of maintaining the computational efficiency of the die-casting computational modeling, the simulation domain usually only includes from the start of the gate position to the entire mold cavity part, and do not need to calculate the liquid metal flow state before entering the gate. This is manifested in the location of the gate, unit time with a certain mass, pressure

of the fluid with a certain speed into the calculation domain, so the need to establish in the location of the gate into the flow boundary conditions. In the paper, the computational domain is divided into two parts: the fluid region and the inflow boundary region, and the particles in each region are fluid particles and inflow region particles, respectively.

2.3.4 Implementation of computational code

In the paper, the calculation code is written in Fortran language and compiled and calculated in CVF6.6 environment. The specific steps to solve the structure of the SPH calculation program for the die-casting filling process are as follows:

(1) Initialize the model. Define each variable used in the calculation, and perform particle division for the wall boundary and inflow region. Particle division can be realized through the program or read in through an external file.

(2) Enter the main loop section. Determine the interacting particle pairs at the current moment and calculate the smooth function and its gradient function.

(3) Calculate the density rate of change according to the continuity equation (18). The obtained pressure value is substituted into the momentum conservation equation (19) and energy conservation equation (20) to obtain the momentum rate of change and energy rate of change.

(4) The density rate of change, momentum rate of change, and energy rate of change obtained in step (3) are time-integrated to obtain the new density, velocity, internal energy, and coordinates of the particle. The time integration adopts the prediction-correction method.

(5) Output the results of the current time step, and at the same time carry out the judgment and update of the incoming boundary, and return to step (2) for the calculation of the next time step.

2.4 Validation and Application of SPH 3D Mathematical Modeling

With the aim of confirming the validity of the SPH-based three-dimensional mathematical model and procedure in this paper, the classical magnesium alloy mechanical problem is simulated and analyzed in this subsection. In this paper, the SPH computed outcomes are benchmarked against the experimental findings from previous studies, and the changes of the wave front position and the water body height at different moments are investigated, and the results are shown in Fig. 1, Fig. 1(a) shows the changes of the wave front position x/H with time T, and Fig. 1(b) shows the changes of the water body height y/H with time T at x=0.

Cross-referencing the modeled outputs with the empirically obtained measurements reveals that the SPH simulation results of this paper are basically consistent with the experimental results, which can accurately describe the three-dimensional dam-busting problem, illustrating the calculation accuracy of this section based on the imaginary particle boundary and the effect of preventing the particles from penetrating the boundary, and verifying the reliability of the three-dimensional computational framework and the procedure written herein, grounded upon the injection-filling methodology of the SPH method.

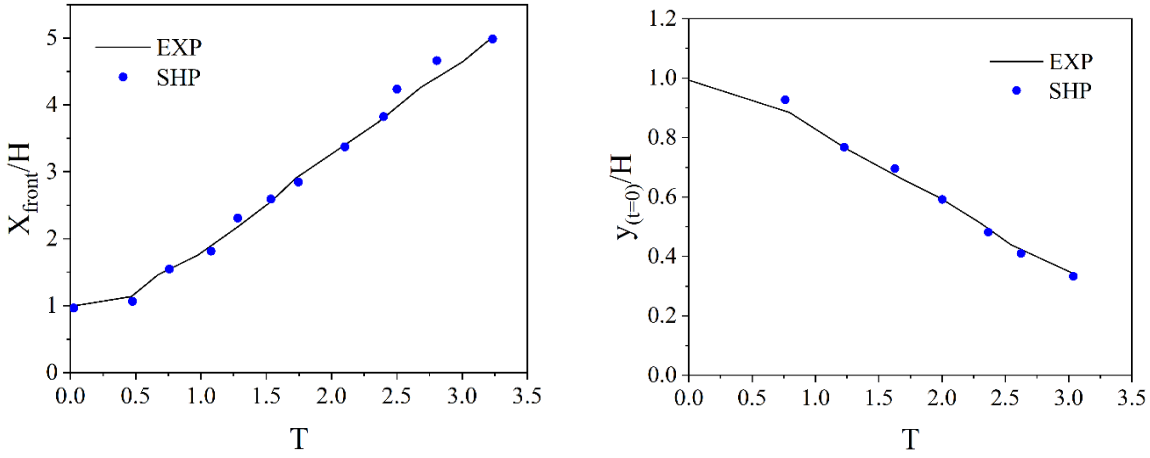

(a) Wavefront position (b) Water height

Figure 1: Comparison of time-dependent SPH simulation results with experimental data

3 Dual-Phase Gas-Melt Flow Modeling within the SPH-Based Cavity-Filling Framework

3.1 3.1 Governing Equation System for Vapor-Liquid Biphasic Flow in SPH Formulation

3.1.1 Control equations for gas-liquid two-phase flow in SPH form

In the casting filling gas-liquid two-phase flow process, need to consider the viscous force of the fluid, pressure, external forces, and gas-liquid cross-consistent equations expressed as follows:

$$\frac{dv}{dt} = -\frac{1}{\rho}\nabla p + \frac{\eta}{\rho}\nabla^2 v + g + \frac{F^s}{\rho} \tag{22}$$

The last term F^s in the above equation is the surface tension, which takes the following mathematical expression:

$$F^s = -\beta k \hat{n} \delta \tag{23}$$

In the above equation, β is the surface tension coefficient, k, $\hat{n}$ are the local geometric curvature and the outward-pointing unit normal at the gas-liquid boundary, respectively, and δ is the Dirac function, which is used to characterize the distribution of surface tension at the gas-liquid interface.

In order to construct the coupling relation linking fluid mass density with the pressure field, it is necessary to introduce an artificial equation of state to couple the solutions of the mass conservation equation and the momentum conservation equation. The artificial equation of state expression for gas-liquid two-phase flow in this paper is as follows:

$$p_x = B\left[\left(\frac{\rho_x}{\rho_0^x}\right)^{\gamma_x} - 1\right] \tag{24}$$

$$p_y = B\left[\left(\frac{\rho_y}{\rho_0^y}\right)^{\gamma_y} - 1\right] \tag{25}$$

$$c_x \geq 10 v_{\max}^x,\ B = \frac{c_x^2 \rho_0^x}{\gamma_x} = \frac{c_y^2 \rho_0^y}{\gamma_y} \tag{26}$$

In the above equation, x for the liquid phase, y for the gas phase, c_x, c_y, respectively, for the liquid phase and the gas phase speed of sound, ρ_0^x, ρ_0^y, respectively, for the liquid phase and the gas phase of the reference density, γ_x and γ_y of the value of the 7 and 1.4, respectively, the liquid phase of the speed of sound c_x is generally taken to be the maximum speed of 10 times the value of the (26) can be found out the value of the initial pressure of B, and then you can find out the value of the gas phase speed of sound c_y.

From the previous Lagrangian control equation of gas-liquid two-phase flow, the SPH form of gas-liquid two-phase flow control equation can be deduced. In this paper, the SPH momentum conservation equation is used, and its discrete form is as follows:

$$\begin{aligned}\frac{dv_i}{dt} = &-\frac{1}{m_i}\sum_j \left(V_i^2 + V_j^2\right)\bar{p}_{ij}\nabla_i W_{ij} + \frac{1}{m_i}\sum_j \frac{2\eta_i\eta_j}{\eta_i + \eta_j} \\ &\times\left(V_i^2 + V_j^2\right)v_{ij}\left(\frac{1}{r_{ij}}\frac{\partial W_{ij}}{\partial r_{ij}}\right) + g + \frac{F_i^s}{\rho_i}\end{aligned} \tag{27}$$

The first term in the above equation is the pressure term, then the average pressure $\bar{p}_{ij}$ between particles is expressed as follows:

$$\bar{p}_{ij} = \frac{\rho_i p_i + \rho_j p_j}{\rho_i + \rho_j} \tag{28}$$

When i and j are same-phase particles, the pressure $\bar{p}_{ij}$ denotes the average pressure between particles, and when i and j are different-phase particles, for the discontinuous density field at the gas-liquid interface, the equation (28) ensures that the $\nabla p / \rho$ term is continuous, and thus the instability of the interface due to the excessively large difference in the density of gas and liquid is solved. The problem. Where the volume $V = m / \rho$, the second term is the discrete form of the viscous force term, the third term is the gravity term, and the fourth term is the surface tension term.

3.1.2 Surface Tension Modeling and Validation

Arising from the difference of van der Waals forces between gas-liquid interfaces, which leads to the existence of interfacial tension at the gas-melt boundary, the contribution of such tension

cannot be neglected when dealing with gas-liquid two-phase flow, so the continuous surface tension model is introduced in this paper.

The defining equation of the color function is as follows:

$$c_l^k = \begin{cases} 1, & l \text{ and } k \text{ are particles of different phases} \\ 0, & l \text{ and } k \text{ are particles of the same phase} \end{cases} \tag{29}$$

Then the expression for the normal vector n_i is as follows:

$$n_i = \nabla c_i = \frac{1}{V_i} \sum_j \left(V_i^2 + V_j^2 \right) \tilde{c}_{ij} \nabla_i W_{ij} \tag{30}$$

Formal:

$$\tilde{c}_{ij} = \frac{\rho_j}{\rho_i + \rho_j} c_i^j + \frac{\rho_i}{\rho_i + \rho_j} c_j^i \tag{31}$$

Then the unit normal vector $\hat{n}_i$ at the interface can be written in the following form:

$$\hat{n}_i = \frac{n_i}{|n_i|} = \frac{\nabla c_i}{|\nabla c_i|} \tag{32}$$

Replacing the Dirac function δ in Eq. (23) with $|\nabla c_i|$ ensures the continuity of the acceleration of the particles at the gas-liquid interface, which in turn ensures the continuity of the velocity of the particles at the gas-liquid interface.

3.1.3 SPH simulation of single bubble upwelling process

In order to validate the reliability of the SPH gas-liquid two-phase flow model, this paper selects the single bubble floating model as the verification example, that is, to simulate the movement process of a two-dimensional circular bubble in still pure water. The radius R of the bubble is set to 0.02m, the height of the fluid calculation domain is set to 10R, the width is set to 6R, and the height from the center of the bubble to the bottom is set to 2R. The basic physical parameters of the SPH method to simulate the uplift of a single bubble are set, the kinetic viscosity coefficient of water η_x is generally $0.001\,Pa \cdot s$, while the ratio of the kinetic viscosity coefficient of air and water is $\eta_y / \eta_x = 0.0177$, the density of water ρ_x is generally $1000\,kg/m^3$, while the ratio of the density of air and water is $\rho_y / \rho_x = 0.001$, the interfacial tension coefficient between the gas and liquid phases is $\beta = 0.0728\,N/m$, and the gravitational acceleration g is generally taken to be $9.81\,m/s^2$, and the number of the total number of fluid particles is 4,453, of which the number of the particles of the water body is 3573, the count of air particles amounts to 235, while the count of boundary particles reaches 596. The total number of fluid particles is 4,453, of which the number of water particles is 3573, the count of air particles amounts to 235, while the count of boundary particles reaches 596. The model uses the CPU IntelCorei7-47903.6GHZ octa-core to perform the parallel computation in about 3.5 hours.

3.2 Gas-liquid two-phase flow modeling of bottom side injection square cavity SPH filling process

In this section, the computational results pertaining to the dual-phase flow behavior throughout the SPH-based injection-filling sequence for bottom-side injected square cavities are benchmarked against the outcomes derived from water simulation laboratory tests to further verify the advantages of the SPH method in dealing with the complex gas-liquid interfaces in the filling process, and the two-dimensional projection diagram of water simulation experiments of bottom-side injected square cavities is shown in Fig. 2.

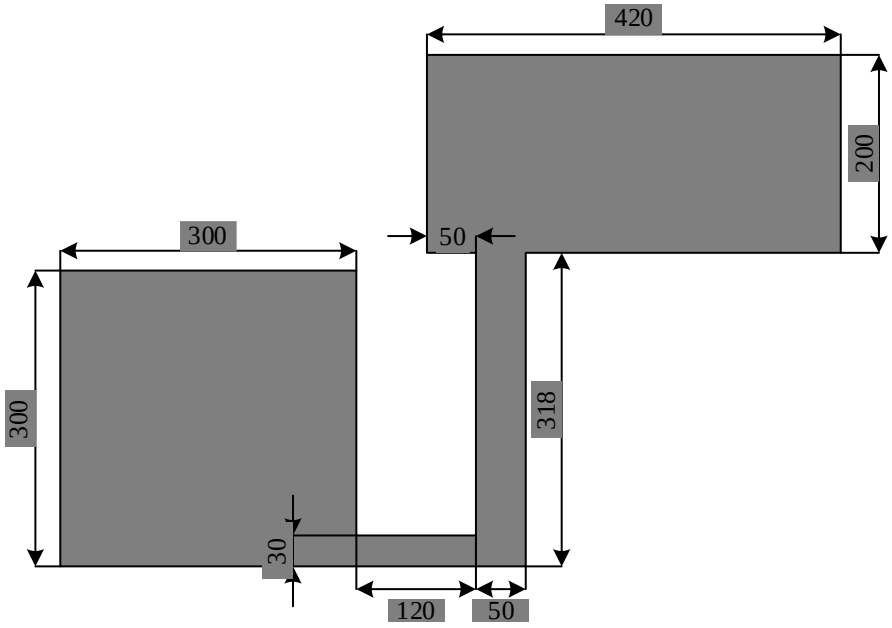

Figure 2: 2D Projection

In the process involving the two-phase gas-liquid flow during the filling calculation of the bottom side injection square cavity, the filling liquid is set to be pure water whose density is $1000\,kg/m^3$ and whose kinetic viscosity coefficient is $0.001\,Pa\cdot s$; the density of the air is $1.2\,kg/m^3$ and the kinetic viscosity coefficient is $1.77\times10^5\,Pa\cdot s$. The total number of particles is 55,219, of which the number of boundary particles is 6,673, the water particle count stands at 27,384, and the air particle count reaches 22,017. The model uses CPU IntelCorei7-47903.6GHZ octa-core to carry out the parallel computation in about 96 hours.

3.3 Modeling analysis of gas-liquid two-phase flow in the filling process

3.3.1 Gas-liquid two-phase flow analysis

Subsequently, the square droplet example is chosen for verification. The established model is shown in Fig. 3, the outer square fluid region has a side length of 2L, the inner side contains a square fluid region with a side length of L, the pressure value of the two is jointly set to $1\,pa$, the density is $\rho_{íâ} = \rho_{ÄÚ} = 1\,kg/m^3$, the dynamic viscous coefficient of the two fluid regions is $\eta_{íâ} = \eta_{ÄÚ} = 0.5$, and the interfacial tension coefficient between the two fluid phases is $\beta = 1$. The influence of gravity is neglected in the whole calculation process of the SPH approach, with the overall particle count being 5,816, among which the inner fluid particle count is 900,

the outer fluid particle count totals 3,528, and the boundary particle count amounts to 1459. 900, the outer fluid particle count totals 3,528, the boundary particle count amounts to 1459, and the smooth length 6 is 2.0 times the particle spacing.

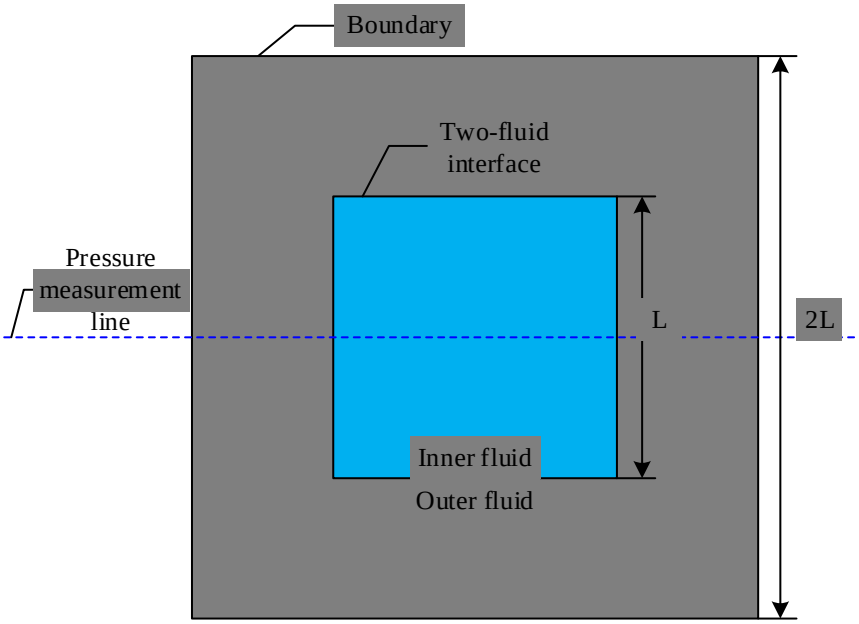

Figure 3: Schematic diagram of surface tension verification model

SPH method surface tension calculation process is shown in Figure 4, Figure 4, the left side of the figure for the two fluid shape; the right side of the figure for the two fluid velocity field diagram; through the SPH method to calculate the density ratio of the two fluids for the above 1:1 in the role of the particle movement under the constructed surface tension model can be seen: the initial state of the two fluids are regularly distributed in the problem domain, when the calculation to 0.06s in the SPH method of surface tension model Calculation of the initial period, from the velocity field calculation charts located in the four corners of the inner square droplet two-phase junction near the particle to the geometric center of the movement, but the horizontal and vertical symmetry centerline particle velocity is zero, stationary; when the calculation of 0.2s, the four corners of the inner square droplet two-phase junction of the particles in the action of the surface tension is gradually to the center of the movement, because of the existence of the particles of the mutual Because of the interaction between the particles, the particles near the horizontal symmetry centerline and the particles near the vertical symmetry centerline move away from the geometrical center, and the distribution of the velocity field in the whole process is very regular without any messy distribution, which also reflects the stability and accuracy of the calculation of the SPH method from the side. After the oscillation and viscous dissipation in the calculation process, the velocity of the fluid particles gradually decreases, and finally comes to a standstill to form the final shape of the circle.

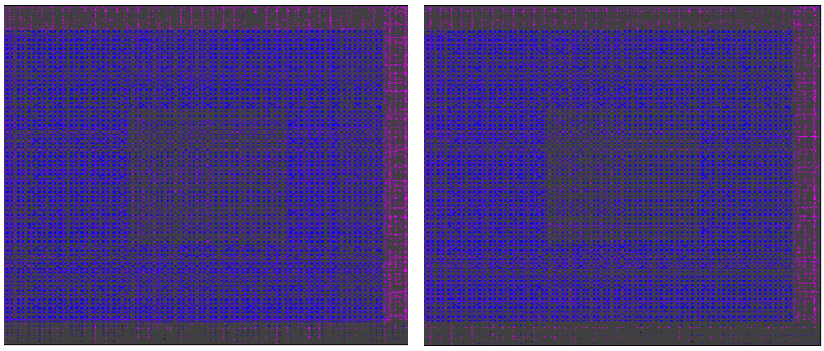

(a) t=0

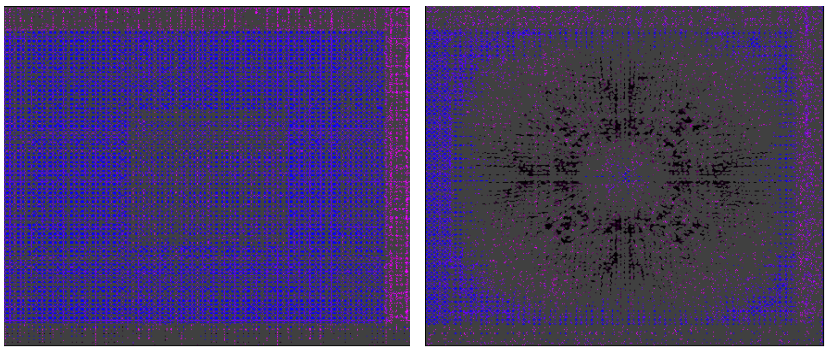

(b) t=0.06s

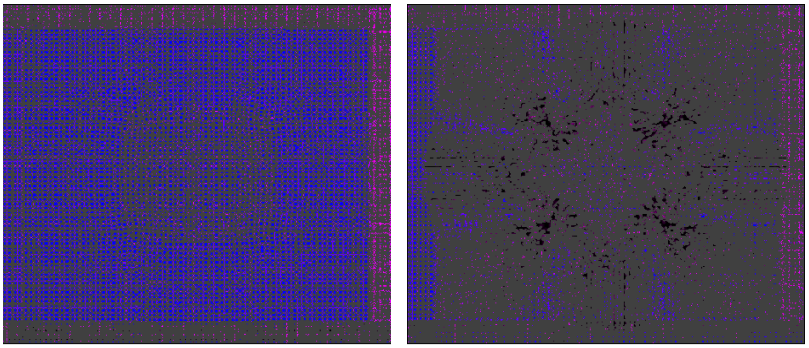

(c) t=0.2s

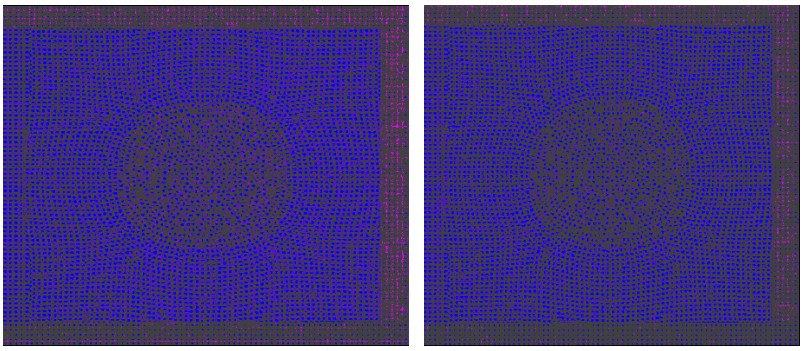

(d) t=1.0s

Figure 4: Calculation process diagram of surface tension of SPH method

At the same time, in the final calculation of the SPH method steady state results graph along the pressure value measurement line from left to right uniformly selected 43 measurement points, extracted the pressure value calculated at the corresponding measurement point, through the calculation of the generalization and organization of the distribution of the graph shown in Figure 5. As can be seen from the figure, the distribution of the pressure values calculated at the 43 measurement points along the pressure value measurement line extracted uniformly from the left to the right in the final calculation of the surface tension model of the SPH method is basically consistent with the analytical equation obtained by calculation, which verifies the correctness of the surface tension model established by the SPH method.

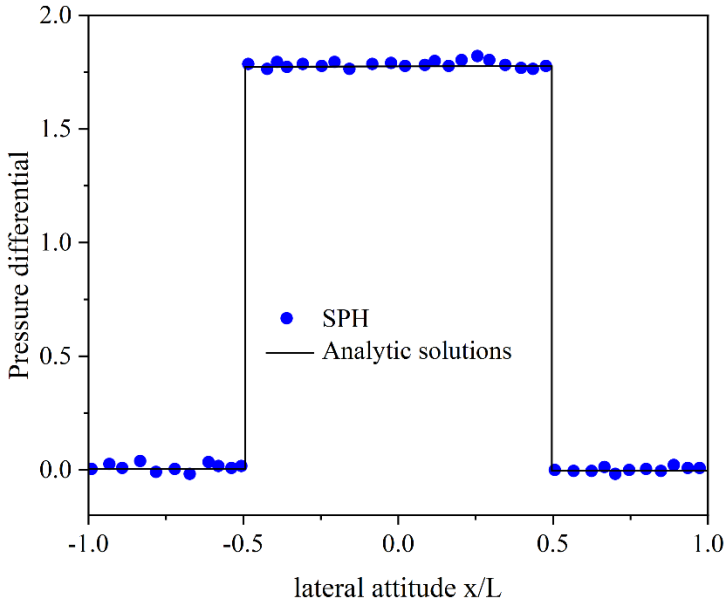

Figure 5: Calculation of transverse distribution of pressure value of two fluid under steady state

3.3.2 Analysis of the process of bubble uplift

With the aim of validating the precision of the constructed SPH surface tension approach applied to computing the gas-liquid dual-phase movement under conditions of substantial density discrepancy, the thickness value at the symmetric place of the center of the bubble and the top displacement value derived from the SPH computational outcomes are extracted, and the resulting extracted data are subsequently benchmarked against the experimental findings.

Through extracting the thickness value and top displacement value at the symmetric place of the bubble center from the SPH numerical computation outcomes, and consolidating the extracted computational findings alongside the experimental results, the outcomes are presented in Fig. 6. The experimental values and the SPH numerical computation findings demonstrate a high degree of agreement, the experimental values are distributed in the SPH method near the calculation results, there is no deviation from the value of a large number of good fit; confirmed through the SPH-based approach that the constructed interfacial tension model is capable of accurately capturing the density contrast between the gaseous and liquid components, and with considerable accuracy, this establishes a computational basis for investigating the gas-liquid flow behavior in the casting process via the SPH methodology. It lays a solid foundation for the research and calculation of SPH method applicable to the two-phase gas-liquid flow problem in the context of the casting procedure.

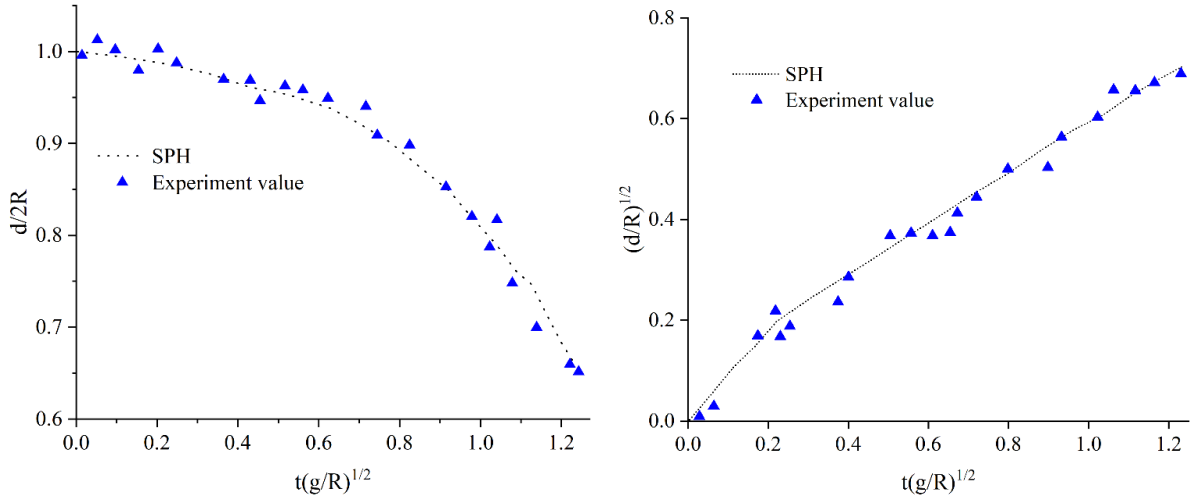

(a) The curve of the thickness of the center of the bubble with time

(b) The motion of the position of the top of the bubble varies with time

Figure 6: Compare results

3.3.3 Liquid bottom side injection square cavity analysis

To further validate the practicality of establishing the SPH method for the two-phase gas-liquid flow behavior occurring within the casting procedure, calculations were carried out for the underwater side injection, and a sketch of the experimental structure of the underwater side injection square cavity is shown in Fig. 7.

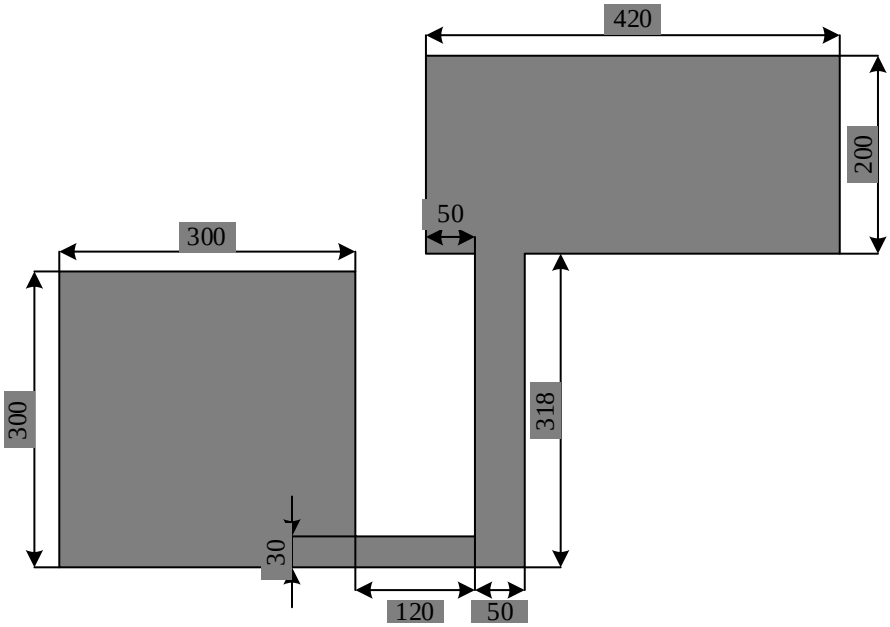

Figure 7: Structure diagram of square cavity with bottom side injection

In the SPH method of calculating the bottom side injection into the square cavity, the liquid is water, $\rho_{\text{Water}} = 1000\ kg/m^3$, $\eta_{\text{Water}} = 0.001\ Pa \cdot s$; $\rho_{\text{Vapor}} = 1\ kg/m^3$, $\eta_{\text{Vapor}} = 1.77 \times 10^5\ Pa \cdot s$. The total number of particles is 57,554, including 34,273 liquid particles and 23,125 air particles, and the smooth length h is 1.5 times the particle spacing.

Calculated and experimental results are shown in Fig. 8, the left graph is the calculated results of the SPH method, and the right graph is the experimental results.

In the left SPH method calculation result diagram, the black area indicates water particles, and the blank area indicates air particles, when the calculation time is 0.37s, the liquid flows into the cavity from the right inner sprue after contacting with the leftmost boundary, and then rises along the boundary, and rises to the top of the liquid at a certain height to move to the right, comparing with the right experimental result diagram, both of them basically coincide with each other. Calculation time 0.58s, in the left side of the SPH method calculation results map, the liquid particles have been flipped to the right, the moment at the same time involved in the air, the formation of the volume of air, and the right side of the experimental results of the map for comparison, the two are in good agreement. Calculation time 1.65s, in the left side of the SPH method calculation results graph, the liquid particle movement into a smooth stage, the whole liquid surface rises smoothly, calculated to fill the cavity, and the right side of the experimental results of the graph for comparison, the two are basically consistent.

SPH method calculation results and experimental results match better, SPH method calculation pertaining to the dual-phase gas-liquid flow injected into a square cavity positioned at the bottom side beneath the water can accurately capture the changes occurring at the gas-liquid interfacial region throughout the calculation procedure, and also calculate the displacement of the gas particles in the process of filling the mold, which in turn lays a theoretical foundation for accurately predicting the defects of magnesium alloy casting process such as rolled gas.

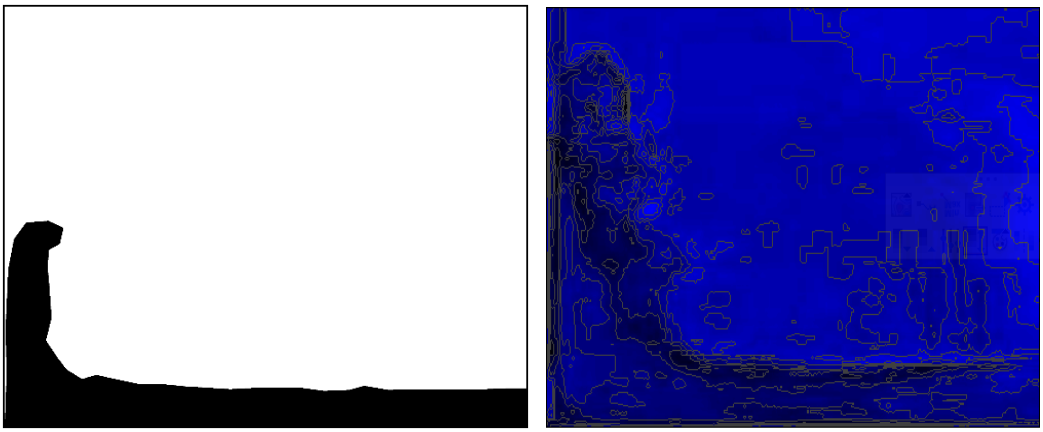

(a) t=0.37s

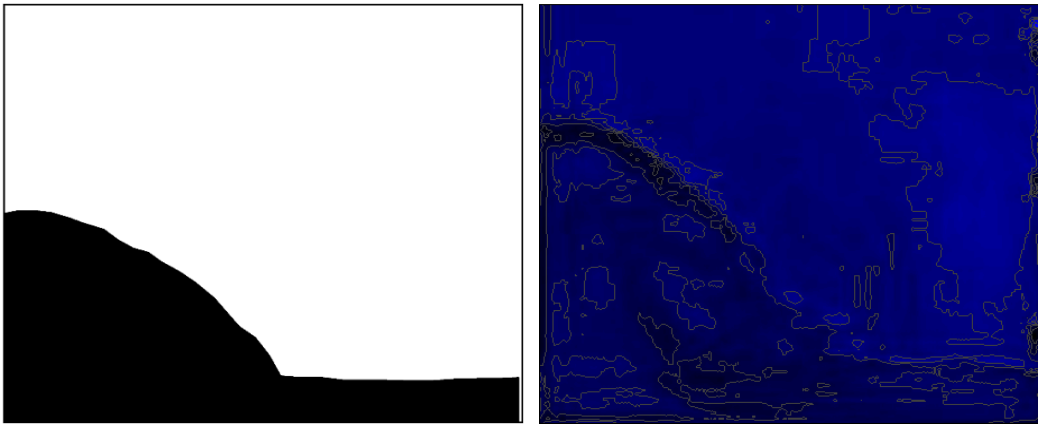

(b) t=0.58s

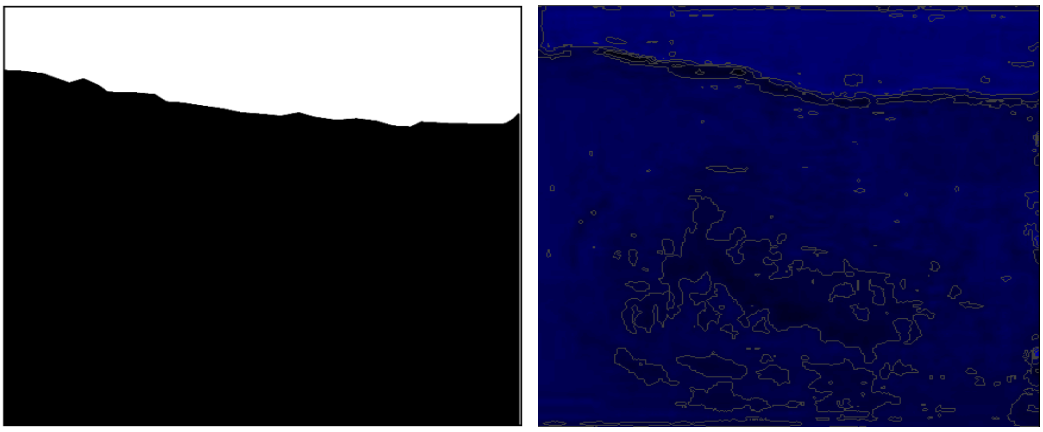

(c) t=1.65s

Figure 8: Comparison of SPH simulation results with experimental datay

4 Influence of different die casting parameters on the flow behavior of the filled molds

During the die casting filling procedure, upon the moment when molten metal is introduced into the pressure chamber, the liquid metal within the chamber tends to generally filled to about 30%~60%, and the rest of the space is filled with air. Slow pressure injection is to make the liquid metal smooth flow, air can be discharged smoothly. But only slow pressure injection, molten metal encounters difficulty in thoroughly occupying the mold cavity. Fast compression injection is aimed at enabling the molten metal to completely fill the mold space smoothly and form qualified die castings. This topic in the pouring temperature are 670 °C, mold temperature are 150 °C conditions to compare the ejection speed were A1 slow ejection 0.2m/s, A2 group slow ejection 0.2m/s, fast 1.2m/s, A3 slow ejection 0.2m/s, fast 1.5m/s of aluminum liquid filling behavior, and compared with the numerical simulation results.

(1) Shooting results

Table 1 shows the metal liquid charging time of A1, A2 and A3 tests. only slow compression shooting but no fast compression shooting in A1 test, its metal liquid flow speed is obviously slowed down compared with A2 and A3 tests, and the charging time differs from A2 and A3 tests, the charging time is longer, which exerts a considerable influence upon the flow behavior of the metal liquid. In the actual shooting results, comparing the filling time of the three groups of tests, the data reveal that the injection velocity of the pressure has a more pronounced bearing on the ability of the liquid metal flow, the faster the pressure injection speed, the shorter the time required for the molten metal to completely occupy the mold cavity.

Table 1: The filling time of aluminum liquid at different injection speed in camera

Test number	Pressurization speed	Filling time (s)
A1	0.3	0.836
A2	0.3, 1.3	0.159
A3	0.3, 1.7	0.112

(2) Simulation results

Table 2 shows the simulated metal liquid filling time of A1, A2 and A3. According to Table 2, it can be obtained that in the computer numerical simulation, the trend of how the pressure

injection speed affects the mold-filling duration is the same as that of the actual shooting, and with the increase of the pressure injection speed, the metal liquid flow speed is accelerated, and its filling time is shortened.

Table 2: The filling time of aluminum liquid at different injection speed in simulation

Simulation number	Pressurization speed	Filling time (s)
B1	0.3	0.672
B2	0.3, 1.3	0.124
B3	0.3, 1.7	0.086

5 Conclusion

The study establishes the SPH method of die casting mold filling process, characterizes the metal liquid flow mold filling behavior of magnesium alloy through visual analysis, and compares with computer numerical simulation to obtain the following results:

(1) The feasibility and accuracy of the mathematical model and calculation procedure of the mold-filling procedure in the die casting context employing the SPH approach in this paper are verified by comparison with the ProCast simulation results and experimental results.

(2) The constructed mathematical framework is applied to reproduce the filling of the bottom-side injection square cavity, and the simulation results show that the established mathematical framework for dual-phase gas-liquid flow within the SPH casting filling process not only can accurately capture the gas-liquid interfaces of the filling process, but also can effectively track the trajectory of the gas particles accompanied by water particles.

(3) The calculation process of the final rounding of two square droplets with a density ratio of 1:1 under the action of surface tension is shown, which confirms the validity of the interfacial tension framework constructed through the SPH approach.

(4) The pressure injection velocity exerts a notable influence upon the filling time, with the faster the pressure injection speed, the shorter the filling time.

References

[1] Reijnders, L. (2024). Are Magnesium Alloys Applied in Cars Sustainable and Environmentally Friendly? A Critical Review. Sustainability, 16(17), 7799.

[2] Bai, J., Yang, Y., Wen, C., Chen, J., Zhou, G., Jiang, B., ... & Pan, F. (2023). Applications of magnesium alloys for aerospace: A review. Journal of Magnesium and Alloys, 11(10), 3609-3619.

[3] Emadi, P., Andilab, B., & Ravindran, C. (2022). Engineering lightweight aluminum and magnesium alloys for a sustainable future. Journal of the Indian Institute of Science, 102(1), 405-420.

[4] Zhang, T., Wang, W., Liu, J., Wang, L., Tang, Y., & Wang, K. (2022). A review on magnesium alloys for biomedical applications. Frontiers in bioengineering and biotechnology, 10, 953344.

[5] Kumar, D., Phanden, R. K., & Thakur, L. (2021). A review on environment friendly and lightweight Magnesium-Based metal matrix composites and alloys. Materials Today:

Proceedings, 38, 359-364.

[6] Stalnichenko, O., Lysenko, T., Ponomarenko, O., Kreitser, K., & Kozishkurt, E. (2024, September). Vacuum Technology for Magnesium Alloys During Die Casting of Radiators. In Grabchenko's International Conference on Advanced Manufacturing Processes (pp. 220-229). Cham: Springer Nature Switzerland.

[7] Panzhong, L., & Ning, L. (2022). Low pressure casting technology and forming process analysis of metal mold based on ProCAST FEA procedure. Mechanics of Advanced Materials and Structures, 29(9), 1308-1315.

[8] Kan, M., Ipek, O., & Koru, M. (2023). An investigation into the effect of vacuum conditions on the filling analysis of the pressure casting process. International Journal of Metalcasting, 17(1), 430-446.

[9] Liu, S. G., Luo, C. B., Li, G. A., Gao, W. L., Lu, Z., & Dai, S. L. (2018). Effect of pressurizing speed on filling behavior of gradual expansion structure in low pressure casting of ZL205A alloy. China Foundry, 15(4), 276-282.

[10] Korti, A. I. N., & Abboudi, S. (2017). Effects of shot sleeve filling on evolution of the free surface and solidification in the high-pressure die casting machine. International Journal of Metalcasting, 11(2), 223-239.

[11] Wang, T., Huang, J., Fu, H., Yu, K., & Yao, S. (2022). Influence of process parameters on filling and feeding capacity during high-pressure die-casting process. Applied sciences, 12(9), 4757.

[12] Ma, C., Wenbo, Y. U., Zhang, T., Zhang, Z., Ma, Y., & Xiong, S. (2023). The effect of slow shot speed and casting pressure on the 3D microstructure of high pressure die casting AE44 magnesium alloy. Journal of Magnesium and Alloys, 11(2), 753-761.

[13] Jiao, X. Y., Wang, J., Liu, C., Guo, Z., Wang, J., Wang, Z., ... & Xiong, S. M. (2019). Influence of slow-shot speed on PSPs and porosity of AlSi17Cu2. 5 alloy during high pressure die casting. Journal of Materials Processing Technology, 268, 63-69.

[14] Yang, J., Liu, B., Shu, D., Li, H., Yang, Q., Hu, T., ... & Tang, X. (2025). Influence of High Injection Speed on Porosity and Mechanical Properties of High-Pressure Die-Casting Al–Si–Mg–Mn Alloy. Metallurgical and Materials Transactions B, 56(5), 5296-5314.

[15] Feng, J., & Xing, B. (2024). Microstructural and mechanical characterization of AM60 alloy in semisolid rheo-die casting with varying injection Velocity. International Journal of Metalcasting, 18(3), 2533-2544.

[16] Ma, Z., Zhang, H., Song, W., Wu, X., Jia, L., & Zhang, H. (2020). Pressure-driven mold filling model of aluminum alloy melt/semi-solid slurry based on rheological behavior. Journal of Materials Science & Technology, 39, 14-21.

[17] Liu, Z. Y., Mao, W. M., Wang, W. P., Zheng, Z. K., & Yue, R. (2017). Investigation of rheo-diecasting mold filling of semi-solid A380 aluminum alloy slurry. International Journal of Minerals, Metallurgy, and Materials, 24(6), 691-700.

[18] Campanella, M., Piccininni, A., & Palumbo, G. (2025). FEM based design of the die cavity to improve the quality of cast parts manufactured via high pressure die casting. The International Journal of Advanced Manufacturing Technology, 1-17.

[19] Li, S., Zhao, S., Li, F., Chang, M., & Wang, Y. (2025). Mold-filling behavior and microstructure evolution of semi-solid 6061 aluminum alloy slurry in die-casting of bracket parts. The International Journal of Advanced Manufacturing Technology, 1-12.

[20] Cao, H., Wang, C., Shan, Q., Che, J., Luo, Z., Wang, L., & Huang, M. (2019). Kinetic analysis of pore formation in die-cast metals and influence of absolute pressure on porosity. Vacuum, 168, 108828.

[21] Kumar, R., & Jha, P. K. (2023). Effect of casting speed on solidification and inclusion motions in bloom mold caster under the influence of in-mold electromagnetic stirring. International Journal of Numerical Methods for Heat & Fluid Flow, 33(3), 1022-1045.

[22] Zhang, H., & Wang, W. (2017). Mold simulator study of heat transfer phenomenon during the initial solidification in continuous casting mold. Metallurgical and Materials Transactions B, 48(2), 779-793.

[23] Liu, Z. (2018). Hydromechanics: Poroelasticity as a Simple Case. In Multiphysics in Porous Materials (pp. 219-235). Cham: Springer International Publishing.

[24] Salary, R., Lombardi, J. P., Samie Tootooni, M., Donovan, R., Rao, P. K., Borgesen, P., & Poliks, M. D. (2017). Computational fluid dynamics modeling and online monitoring of aerosol jet printing process. Journal of Manufacturing Science and Engineering, 139(2), 021015.

[25] Zhang, Y., & Zhang, J. (2019). Modeling of solidification microstructure evolution in laser powder bed fusion fabricated 316L stainless steel using combined computational fluid dynamics and cellular automata. Additive Manufacturing, 28, 750-765.

[26] Rahman, M. S. (2024). Computational fluid dynamics for predicting and controlling fluid flow in industrial equipment. European Journal of Advances in Engineering and Technology, 11(9), 1-9.

[27] Duan, W., Yang, Y., Liu, W., Zhang, Z., & Cui, J. (2022). Modelling the fluid flow, solidification and segregation behavior in electromagnetic DC casting of magnesium alloy. Simulation Modelling Practice and Theory, 115, 102460.

[28] Lopes, V., Pereira, J., Carneiro, V. H., & Puga, H. (2017, February). Magnesium alloy biodegradable scaffolds: Simulation of casting and manufacturing. In 2017 IEEE 5th Portuguese Meeting on Bioengineering (ENBENG) (pp. 1-4). IEEE.

[29] Viswanath, A., Manu, M. V., Savithri, S., & Pillai, U. T. S. (2017). Numerical simulation and experimental validation of free surface flows during low pressure casting process. Journal of Materials Processing Technology, 244, 320-330.

[30] Saeedipour, M., Schneiderbauer, S., Pirker, S., & Bozorgi, S. (2014). A numerical and experimental study of flow behavior in high pressure die casting. In Magnesium Technology 2014 (pp. 185-190). Cham: Springer International Publishing.

[31] Dou, K., Lordan, E., Zhang, Y. J., Jacot, A., & Fan, Z. Y. (2020). A complete computer aided engineering (CAE) modelling and optimization of high pressure die casting (HPDC) process. Journal of Manufacturing Processes, 60, 435-446.

[32] Saucedo-Zendejo, F. R., Reséndiz-Flores, E. O., & Kuhnert, J. (2019). Three-dimensional flow prediction in mould filling processes using a GFDM. Computational Particle Mechanics, 6(3), 411-425.

[33] Gautam, S. K., Roy, H., Lohar, A. K., & Samanta, S. K. (2023). Studies on mold filling behavior of Al–10.5 Si–1.7 Cu Al alloy during rheo pressure die casting system. International Journal of Metalcasting, 17(4), 2868-2877.

[34] Zhang, Y., Jiao, P., Du, W., Qi, G., & Chen, B. (2025). Numerical Simulation of Casting Filling Process Based on SPH-FEM Coupling Method. Symmetry, 17(4), 494.

[35] Cao, H., Shen, C., Wang, C., Xu, H., & Zhu, J. (2019). Direct observation of filling process and porosity prediction in high pressure die casting. Materials, 12(7), 1099.

[36] Cao, H., Zhang, Q., Zhu, W., Cui, S., Yang, Q., Wang, Z., & Jiang, B. (2024). Study on the influence of injection velocity on the evolution of hole defects in die-cast aluminum alloy. Materials, 17(20), 4990.

[37] Szucki, M., Suchy, J. S., Lelito, J., Malinowski, P., & Sobczyk, J. (2017). Application of the lattice Boltzmann method for simulation of the mold filling process in the casting industry. Heat and Mass Transfer, 53(12), 3421-3431.

[38] Puga, H., Barbosa, J., Azevedo, T., Ribeiro, S., & Alves, J. L. (2016). Low pressure sand casting of ultrasonically degassed AlSi7Mg0. 3 alloy: Modelling and experimental validation of mould filling. Materials & Design, 94, 384-391.

[39] Sultana, N., Rafiquzzaman, M., Rahman, Y., & Das, A. (2018). Solidification and filling related defects analysis using casting simulation technique with experimental validation. International Journal of Mechanical Engineering and Applications, 6(6), 150-160.

[40] Battaglia, E., Bonollo, F., Timelli, G., Fiorese, E., & Kral, G. (2017). Correlation between process, microstructure and properties in high pressure die casting aluminium-silicon alloys. Advances in Materials and Processing Technologies, 3(1), 111-124.

[41] Liu, S. G., Cao, F. Y., Zhao, X. Y., Jia, Y. D., Ning, Z. L., & Sun, J. F. (2015). Characteristics of mold filling and entrainment of oxide film in low pressure casting of A356 alloy. Materials Science and Engineering: A, 626, 159-164.

[42] Bandara, A., Kan, K., Yusuke, K., Soga, N., Katsuyuki, T., Koike, A., & Aoki, T. (2024). Micro X-ray Computed Tomography and Machine Learning Assessment of Impregnation Efficacy of Die-Casting Defects in Metal Alloys. Sensors & Materials, 36.

[43] Trometer, N., Godlewski, L. A., Prabhu, E., Schopen, M., & Luo, A. A. (2024). Effect of vacuum on die filling in high pressure die casting: water analog, process simulation and casting validation. International Journal of Metalcasting, 18(1), 69-85.